IAC-20-A6.2.3.x60345

Risk Assessment of Recent High-Interest Conjunctions

Salvatore Alfano[a], Daniel Oltrogge[b], Holger Krag[c], Klaus Merz[d], Robert Hall[e]

[a] *Center for Space Standards and Innovation, Colorado Springs, CO, USA; salfano@centerforspace.com*
[b] *Center for Space Standards and Innovation, Colorado Springs, CO, USA; oltrogge@centerforspace.com*
[c] *European Space Agency, Darmstadt, Germany; Holger.Krag@esa.int*
[d] *European Space Agency, Darmstadt, Germany; klaus.merz@esa.int*
[e] *Technical Director SSA, COMSPOC; rhall@agi.com*

Abstract

There have been several recent high-profile space events, notably the conjunctions of the Aeolus and Starlink spacecraft (both maneuverable) and the IRAS and GGSE-4 spacecraft (both dead). Here, we examine the timeline, activities, and risks associated with each of these conjunction events. To accomplish this, we fused observations from the Space Surveillance Network (SSN) to produce a sequence of high-accuracy orbit solutions and used that sequence to generate three-dimensional, dynamic progressions of each conjunction's miss distance, collision probability and its relation to the dilution threshold. Probability of Collision (Pc) is an essential tool for assessing conjunction threats. The Pc Topology tool characterizes the evolution of a conjunction's miss distance and collision probability, both of which are critical inputs to the maneuver avoidance decision-making process and exposing SSA deficiencies.

The European Space Agency commanded the Aeolus spacecraft to perform an emergency maneuver to avoid this high-probability collision hazard. Our results indicate that this maneuver was warranted based upon ESA's decision threshold criteria and the Pc Topology trending analysis. While both collision events fortunately did not occur, we estimated the potential debris fields that these events may have generated had they occurred. We then assessed the impact of these fragmentation fields upon estimated operator workload and subsequent collision risk.

1. Introduction

As we enter the so-called "New Space" era with the introduction of Large Constellation (LC) spacecraft, the effective mitigation of collision threats is of increasing importance. Although we are only a year into the realization of LCs, a 2019 study by the European Space Agency (ESA) found that approximately 18% of the conjunctions that ESA spacecraft experience involve LC spacecraft and an additional 20% involve small satellites.[1] Given the expected dramatic increase in the number of close approaches and collision threats[2], it is critical that we not only ensure that Space Situational Awareness (SSA) and Space Traffic Coordination and Management (STCM) regimes are fielded and available, but also that we ensure that the resulting SSA and STCM products and services are effective and relevant.

There have been several recent high-profile space events, notably the conjunctions of the Aeolus and LC Starlink spacecraft (both maneuverable) and the IRAS and GGSE-4 spacecraft (both dead). In this paper, we examine the timeline, activities, and risks associated with each of these conjunction events, considering how communications, better SSA data, and improved risk assessment and trending tools can help our future New Space flight safety.

To accomplish this for both conjunctions, we fused observations from the Space Surveillance Network (SSN) to produce a sequence of high-accuracy orbit solutions and used that sequence to generate three-dimensional, dynamic progressions of each conjunction's miss distance, collision probability and its relation to the dilution threshold. Probability of Collision (Pc) is an essential tool for assessing conjunction threats.

We then applied the Pc Topology Tool[3] (U.S. Patent No 10558320) to fully characterize the evolution of a conjunction's miss distance and collision probability, both of which are critical inputs to the maneuver avoidance decision-making process and exposing SSA deficiencies.

While both collision events fortunately did not occur, we estimated the potential debris fields that these events may have generated had they occurred. We then assessed the impact of these fragmentation fields upon estimated operator workload and subsequent collision risk.

2. Methodology

When performing conjunction analysis, it is often the case that the orientation and configuration/shape of the satellites are unknown. It is almost exclusively the case for debris objects. This necessitates certain assumptions when computing collision probability. A common practice is to approximate a spacecraft's hardbody with an encapsulating sphere. This one-shape-fits-all approach eliminates the need to determine orientation, but results in an overestimated object volume and an overinflated probability unless both satellites are actually spheres.

To produce more representative probabilities, we use a satellite's dimensions to define a rectangular box. This more accurately portrays the actual collision threat by projecting a smaller area than a sphere, the downside is that the box's orientation must be known. To address this, we provide a spectrum of values for all possible orientations based on uniformly-spaced viewing angles. The user then has the freedom to choose a suitable range of orientations. Even when choosing the maximum footprint possible, the resulting probability of the box will be less than that of the sphere.

Figure 1 shows a box of length (l), width (w), height (h) with Aeolus dimensions of [13m, 4.3m, 1.6m] (https://discosweb.esoc.esa.int/, subscription required) placed inside a sphere populated with evenly spaced viewing points. For what follows, it is always assumed that $l \geq w \geq h$.

The first step in this sampling process is to generate equally-distributed viewing points on the surface of a sphere in order to observe a rectangular box. The three-dimensional box is viewed from all points to determine the associated two-dimensional, projected, surface areas as they would appear in a probability encounter plane. These resulting areas are then sorted in ascending order and their cumulative representation displayed as a monotonically increasing distribution in Figure 2.
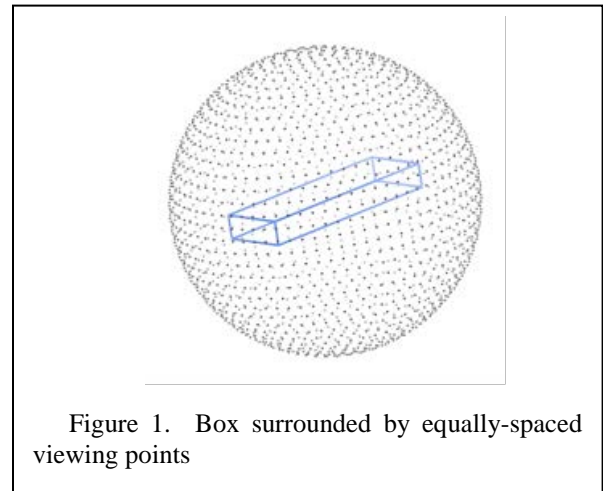

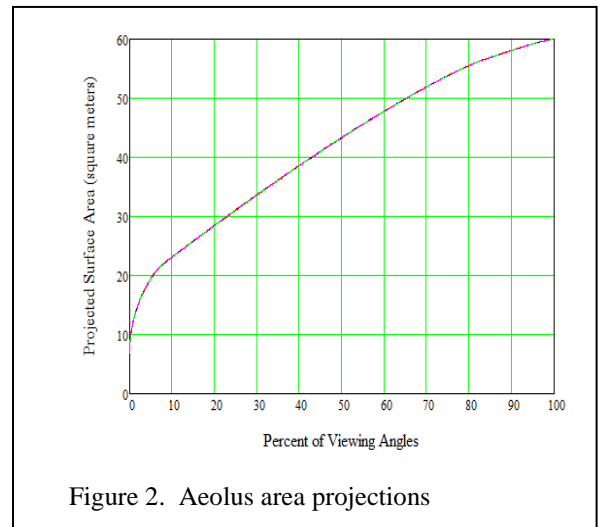Figure 1. Box surrounded by equally-spaced viewing points

Figure 2. Aeolus area projections

As shown in Figure 2, 80% of the viewing angles will observe a surface area at or below 56m[2], 50% below 44m[2], and so on. The associated radii for representative circles in the encounter plane are computed using a method similar to Chan's Method of Equivalent Cross-Sectional Area (MECSA)[4]. Unlike Xie and Chan's approach, the rectangular dimensions and orientation are redefined in the encounter plane rather than converting to a circle, thus simplifying the integrable region. The resulting radius distribution is shown in Figure 3.

From Figure 1 and Figure 2, we see that the box's largest projected area is 60m[2] which will produce a circle of equivalent area with radius of 4.37m.

Figure 3. Radii of Aeolus area projections
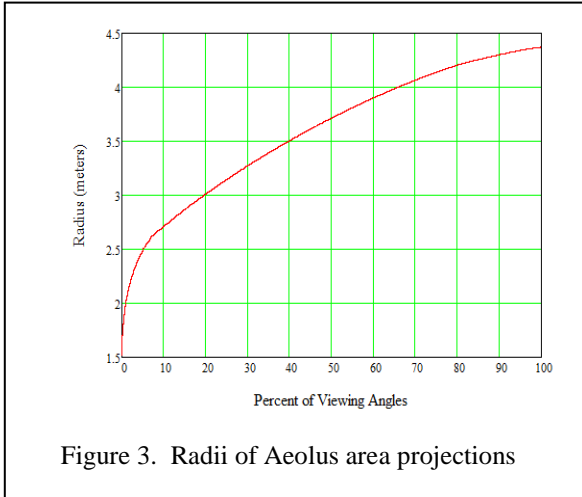
To contrast this with a satellite's representation as an encapsulating sphere, Figure 4 shows a sphere of minimal volume that touches all corners of the same Aeolus box.

Figure 4. Sphere of minimal volume touching all corners of box
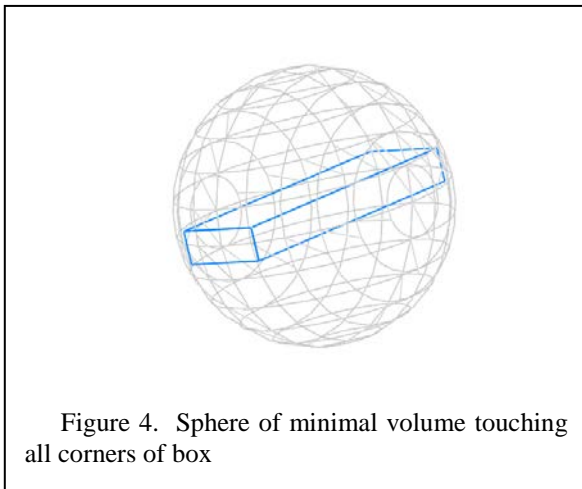
The sphere's diameter is 6.89m with a projected area of 149.3 m^2 regardless of viewing angle. In the encounter plane, such a circle will envelop the largest possible Aeolus box plus an additional 89.3 m^2 of density space. Thus, for the same centroid, the box's smaller footprint will produce a lower and more reasonable probability. This holds true for all cases because the encapsulating circle will always contain more probability density space than a box's projected maximum area.

Figure 5. Starlink area projections
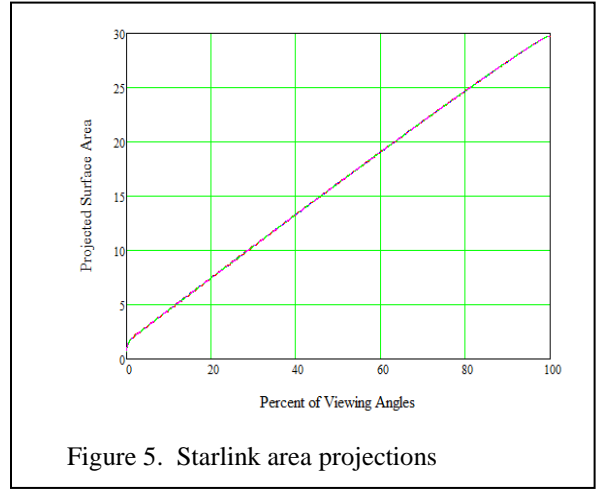
This entire process is repeated using the conjuncting satellite's dimensions to produce its projected areas/radii. For this work, Starlink's box dimensions [9m, 3.3m, 0.2m] result in a maximum projected area of 29.8 m^2 and an encapsulating sphere radius of 4.79m.

Figure 6. Radii of Starlink area projections
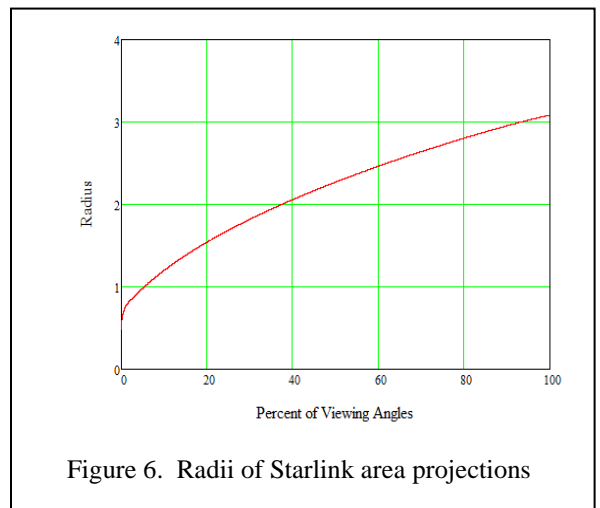
The minimum, maximum, and/or user-choice percentages of the box are used to establish their respective radii. When modeling an encapsulating sphere, its radius is used instead. Summing the radii for both objects determines the combined hardbody radii (CHBRs) for all 3 cases.

It is convenient to rotate the encounter plane so that its x axis is aligned with the covariance major axis to

eliminate cross covariance terms while also ensuring $\sigma x \geq \sigma y$. Collision probability computation requires the MECSA CHBR, the standard deviations $[\sigma x \ \sigma y]$, and the rotated miss distance vector $[xm \ ym]$ which defines the centroid.

$$Pc_{circle} = \frac{1}{2\pi\sigma_x\sigma_y} \int_{-CHBR}^{CHBR} \int_{-\sqrt{CHBR^2-x^2}}^{\sqrt{CHBR^2-x^2}} exp\left[\frac{-1}{2}\left\{\left(\frac{x+xm}{\sigma_x}\right)^2 + \left(\frac{y+ym}{\sigma_y}\right)^2\right\}\right] dydx \quad (1)$$

Although this equation cannot be solved analytically, there are many numerical techniques available to adequately approximate it[5,6,7,8,9,10,11].

Rather than using a circle of equal projected area, one can define a rectangle[12,13,14,15,16] in the same covariance-aligned encounter plane. Recalling that $l \geq w \geq h$, we define the length of a rectangle's side associated with the maximum projected area is

$$s_{max} = \sqrt{l^2 + w^2} \ . \quad (2)$$

The side associated with the minimum projected area s_{min} will have a length

$$s_{min} = w \ . \quad (3)$$

Any length s in between its minimum and maximum will be scaled linearly according to the percent of viewing angles. The projected area a_{proj} associated with that percentage determines the length of the rectangle's other side s_{other} as

$$s_{other} = \frac{a_{proj}}{s} \ . \quad (4)$$

For a rectangle whose sides are parallel to the covariance axes, x is not dependent on y. This allows a decoupling of the probability equation and subsequent analytical expression.

$$Pc_{rectangle} = \left|\frac{1}{2}\left\{erf\left(\frac{xm+s}{\sqrt{2}\sigma_x}\right) - erf\left(\frac{xm-s}{\sqrt{2}\sigma_x}\right)\right\}\right|$$

$$\times \left|\frac{1}{2}\left\{erf\left(\frac{ym+s_{other}}{\sqrt{2}\sigma_y}\right) - erf\left(\frac{ym-s_{other}}{\sqrt{2}\sigma_y}\right)\right\}\right| \quad (5)$$

Due to the many and varied relationships between the relative distances, standard deviations, and rectangle sizes, this equation must be evaluated twice: once as

shown and again with the values of s and s_{other} switched. The maximum of the two results should then be chosen.

Alternatively, one can use a square of equal projected area with its sides parallel to the covariance axes in the encounter plane. This is somewhat simpler as the dimensions become

$$s = s_{other} = \sqrt{a_{proj}} \ . \quad (6)$$

By symmetry, no switching is required. Obviously, such substitutions will create different footprints in the conjunction encounter plane.

These values are then depicted on the topology using the representation for each instance of a conjuncting pair shown in Figure 7.
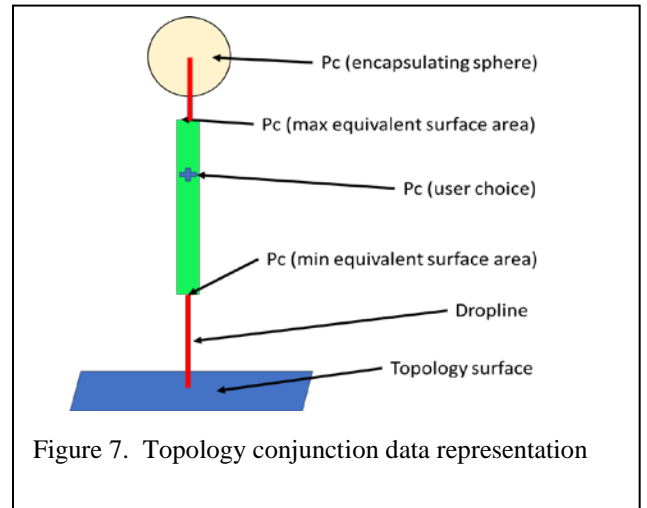

Figure 7. Topology conjunction data representation

3. AEOLUS/STARLINK Conjunction

ESA commanded the Aeolus spacecraft to perform an emergency maneuver to avoid this high-probability collision hazard. As we will show in this section, our results indicate that this maneuver was warranted based upon ESA's decision threshold criteria and the Pc Topology trending analysis.

US data predicted a close approach between ESA's AEOLUS (NORAD ID 43600) satellite and SpaceX's STARLINK 44 (NORAD ID 44261), forecast to occur on September 2, 2019, 11:02 GMT at an altitude of 320 km. Both ESA and SpaceX were using conjunction information from the 18th Space Control Squadron (SCS). ESA's Space Debris Office calculated the collision probability, combining information on the expected miss distance, conjunction geometry, and uncertainties in orbit information while treating the objects as spheres. As time passed, the probability of collision continued to increase. When the probability

exceeded 1 in 1000, ten times higher than their threshold, ESA determined an avoidance maneuver was warranted and subsequently executed.

The Commercial Space Operations Center (ComSpOC, https://www.agi.com/comspoc) independently processed the USAF Space Surveillance Network raw observation measurements to produce its own orbit solutions & conjunction assessment. No Two-Line Elements or Special Perturbations vectors from the 18th SCS were used. Using progressive updates of position, velocity, and covariance data provided by the ComSpOC, Table 1 and Table 2 contrast the maximum and minimum Pc values, respectively, when modeling the satellites as spheres versus other, judiciously-reduced shapes. For an encapsulating sphere, the probability grows to be greater than ESA's threshold of 1 in 1000.

Table 1. AEOLUS/STARLINK maximum projections of MECSA circle, box, and rectangle for equivalent areas.

Hours to TCA	Pc (encapsulating sphere)	Pc (MECSA circle)	Pc (square)	Pc (rectangle)
72	0.00007371	0.000029954	0.000029953	0.000029957
48	0.00027628	0.000112808	0.000112789	0.000113070
24	0.00067013	0.000273487	0.000273446	0.000274059
12	0.00225403	0.000918030	0.000917955	0.000919046
6	0.00075473	0.000305757	0.000305786	0.000306973
4	0.00168842	0.000684202	0.000684262	0.000686749
2	0.00175648	0.000711596	0.000711664	0.000714526
1	0.00175648	0.000711596	0.000711664	0.000714526
0	0.00020659	0.000083425	0.000083441	0.000084224

Table 2. AEOLUS/STARLINK Minimum projections of MECSA circle, box, and rectangle for equivalent areas.

| Hours to TCA	Pc (encapsulating sphere)	Pc (MECSA circle)	Pc (square)	Pc (rectangle)
72	0.00007371	0.000002028	0.000002028	0.000002351
48	0.00027628	0.000007662	0.000007662	0.000008883
24	0.00067013	0.000018570	0.000018570	0.000021529
12	0.00225403	0.000062254	0.000062254	0.000072167
6	0.00075473	0.000020662	0.000020662	0.000023963
4	0.00168842	0.000046245	0.000046246	0.000053632
2	0.00175648	0.000048089	0.000048089	0.000055772
1	0.00175648	0.000048089	0.000048089	0.000055772
0	0.00020659	0.000005626	0.000005626	0.000006529
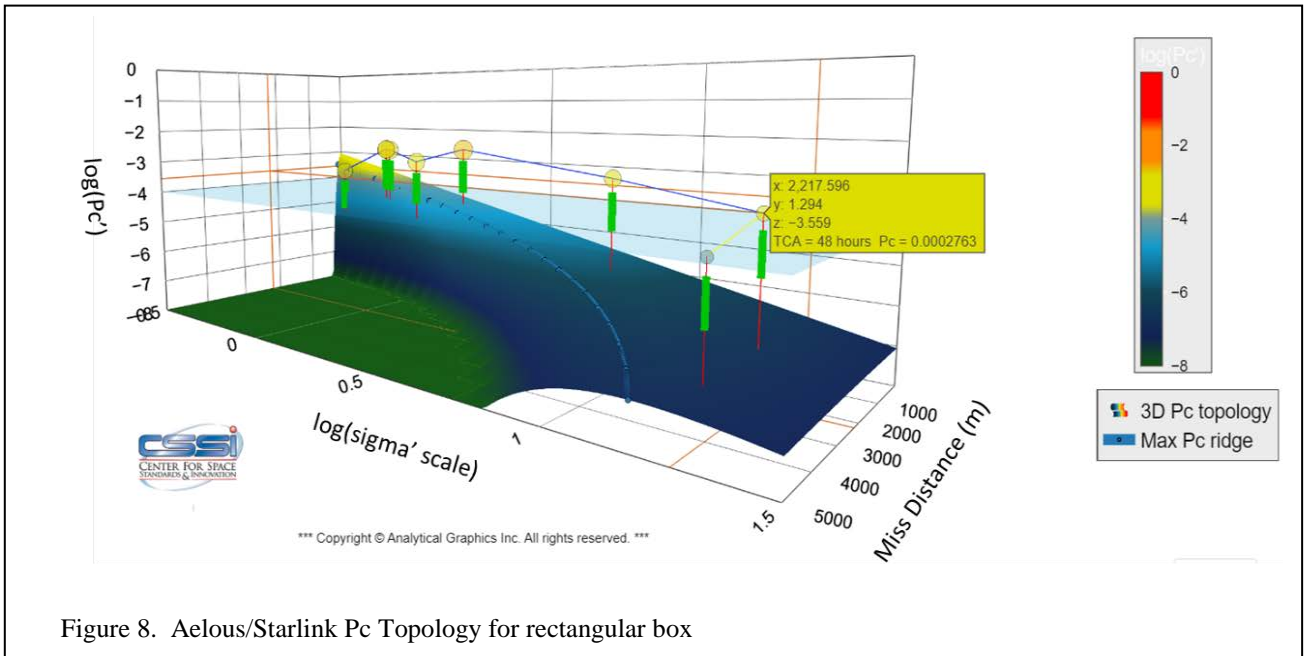
Figure 8. Aelous/Starlink Pc Topology for rectangular box

As the tables show, the satellites' equivalent projected areas produce considerably lower probabilities than encapsulation by eliminating density space. The box enveloping the satellite is not an exact representation and will, itself, contain some empty space. To eliminate that remaining empty space would require precise knowledge of both satellites' configurations and relative orientations using more refined techniques[17,18,19].

This tabular data can be easily viewed in the Probability (Pc) Topology Tool, showing the relationship between probability, covariance size, and miss distance for an object's size and shape. Decision-makers often find that understanding/visualizing these relationships is very useful when determining whether an avoidance maneuver is warranted. Covariance scale and miss distance are varied to create a probability contour showing the evolution of a conjunction.

An interactive HTML file is created for viewing with any web browser, making it readily shareable with the customer. The HTML page shown in Figure 8 enables the user to interactively reorient the three-dimensional plot and/or zoom in/out. A maximum probability ridge line shows the dilution region boundary. Pc estimates are in this region (as shown in the following figure) whenever the contour's downward slope corresponds to an increasing covariance size. A user-defined

probability threshold plane (translucent, blue) is also included so that one can determine if Pc is above or below a prescribed action threshold. With such a visualization, one can readily assess the distance and/or covariance scale (displayed as logarithm to the base 10) required to reduce probability below the threshold.

The snapshot of the AEOLUS/STARLINK topology (Figure 8) displays the sequence of probabilities, trending the conjunction's evolution through the series of orbital updates which accompanied the orbital geometry and evolution leading up to that conjunction. This topological analysis shows that this incident had a sustained high probability of collision throughout the entire sequence of Pc assessments, even when high quality orbit determination data and data fusion analytics were employed by the ComSpOC. The fact that the final Pc estimates were above ESA's decision threshold criteria, and that the Pc topology trending analysis shows these probabilities to be accompanied by great confidence in predicted miss distance, indicates that an avoidance maneuver was warranted.

Note that the range of equivalent-area probabilities $Pc_{rectangle}$ (in green) are always below the encapsulation values (filled "balloons"). Probability is presented on a logarithmic scale, therefore the 50th percentile of viewing angles will not be the midpoint of the green bar. Each probability "balloon" is color-coded

and sized based on its value. All but the first two (oldest) balloons are linked together by blue lines to show their time-ordered sequence. The first two balloons are linked by a yellow line to reveal the starting point. Since each update produces a unique contour and maximum ridge line, it would be confusing to show all of them at once. Instead, a single, representative, hybrid contour is shown beneath all the probability balloons (Pc topo paper here). Red vertical lines connect the probability balloons to the surface, revealing their proper relation to their relative maximums. By hovering the pointer anywhere over the contour, a pop-up window reveals the miss distance, hybrid covariance scaling, and hybrid probability value. For that pointer location, a corresponding orange line is projected to each axis. If hovering over a balloon, the Time until Close Approach (TCA) is also included as well as the estimated actual probability.

Figure 9 shows annual encounter rates for all active satellites from the Resident Space Object Catalog (RSO) versus publicly available RSO debris for October 29, 2019. This particular catalog was chosen for consistency with a previous publication[2] and provides the baseline collision risk to the ensemble of operational satellites in LEO (~2,250 PLs) before the event.

The DEBBIE collision and explosion fragmentation tool[20,21] was used to model the ensemble of debris fragments that could have been generated were this collision have been allowed to occur. For this simulation, we adopted a 30% involvement and a mass of 1358 kg by Aeolus, and a 20% involvement and a mass of 227 kg by Starlink. From this DEBBIE simulation, it was estimated that 10,658 fragments larger than 1 cm in characteristic length could have been generated from an Aeolus/Starlink collision should an effective mitigation strategy not been followed, and these individual fragments were each assigned notionally-representative post-fragmentation orbits.
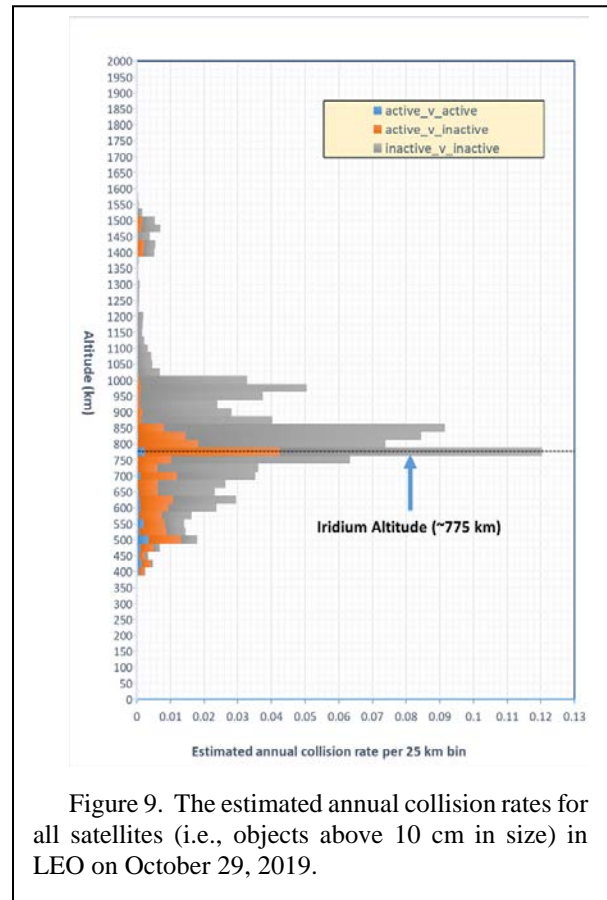

Figure 9. The estimated annual collision rates for all satellites (i.e., objects above 10 cm in size) in LEO on October 29, 2019.

Figure 10 depicts the additional annual encounter rates introduced solely by this collision-induced debris (i.e., augmenting the previous chart), using AGI's "Probability and Frequency of Orbital Encounters" tool (U.S. Patent No 10293959) to assess collision rates with these 10,658 debris fragments. The details of which can be found in the paper "Volumetric assessment of satellite encounter rates."[22] These charts assume no remediation or attempt at future avoidance.

A key take-away from Figure 10 is that not only are encounter rates at the collision's altitude of 320 km above a spherical Earth (occurring during Starlink's early orbit ascent phase) dramatically increase from zero to 0.0175 per year, but collisions with spacecraft in the 400 to 450 altitude bin are likely to increase fivefold.
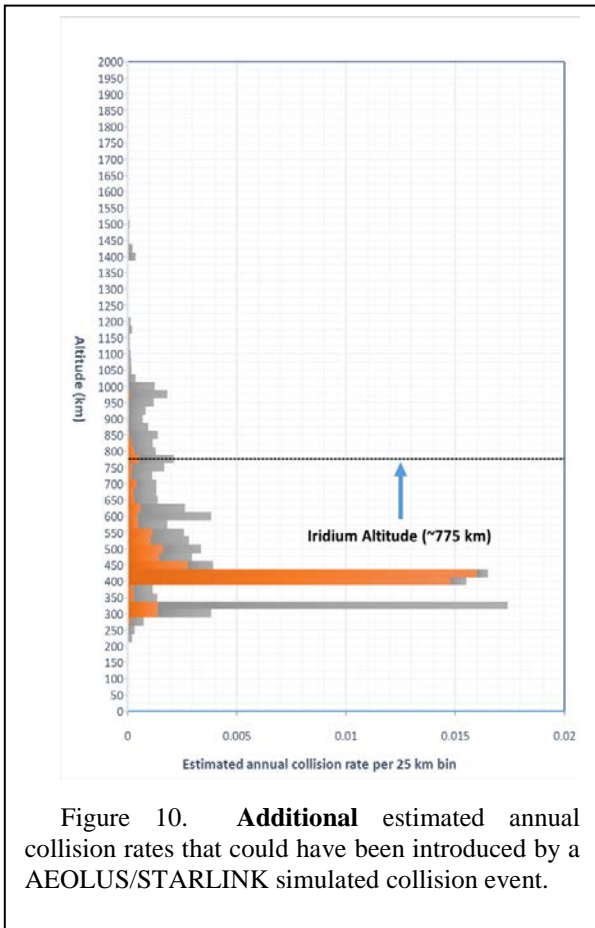
Figure 10. **Additional** estimated annual collision rates that could have been introduced by a AEOLUS/STARLINK simulated collision event.

4. IRAS/GGSE-4 Conjunction

US data predicted a close approach between the Infrared Astronomical Satellite (IRAS, NORAD ID 13777) satellite and the Gravity Gradient Stabilization Experiment (GGSE-4, NORAD ID 02828), forecast to occur on January 29, 2020, 23:39 GMT at roughly 900 km altitude. Both satellites were inoperable and therefore incapable of maneuvering. Progressive conjunction information from the 18th SCS repeatedly showed a miss distance under 20m. Had the collision occurred, the 1,083 kg IRAS and the 85 kg GGSE-4 would likely have generated hundreds of pieces of debris in a well-populated orbit regime.

IRAS's box dimensions [3.6m, 3.6m, 2.05m] and GGSE-4's dimensions [18m, 0.7m, 0.6m] were used along with 18th SCS orbital data to produce the following tables. GGSE-4's encapsulating sphere was quite large due to its long protruding boom. This made it a good candidate to compare and contrast with the box's equivalent area representations.

As in the previous example, Table 3 and Table 4 show that the satellites' equivalent projected areas produce considerably lower probabilities than encapsulation by eliminating density space. GGSE-4's elongated shape causes a large difference between maximum and minimum projected areas, resulting in a large range of associated Pc values readily seen in the corresponding Pc Topology for a rectangular box depicted in Figure 11.

Table 3. IRAS/GGSE-4 Maximum projections of MECSA circle, box, and rectangle for equivalent areas.

Days to TCA	Pc (encapsulating sphere)	Pc (MECSA circle)	Pc (square)	Pc (rectangle)
1.266	0.1167143445	0.017260965	0.017299653	0.02389743
1.143	0.0476081306	0.004080373	0.004117668	0.00485467
1.080	0.0459504180	0.002953580	0.002998838	0.00357318
0.922	0.0964306261	0.006623827	0.006707098	0.00679384
0.757	0.0539821186	0.003011891	0.003061938	0.00328097
0.592	0.0485720478	0.001102647	0.001108288	0.00058157
0.430	0.0451860561	0.000855586	0.000859203	0.00041743
0.268	0.0524852095	0.001079511	0.001092967	0.00060388
0.095	0.0268969401	0.000186707	0.000204474	0.00901497

Table 4. IRAS/GGSE-4 Minimum projections of MECSA circle, box, and rectangle for equivalent areas.

| Days to TCA	Pc (encapsulating sphere)	Pc (MECSA circle)	Pc (square)	Pc (rectangle)
1.266	0.1167143445	0.002832073	0.002833200	0.00387616
1.143	0.0476081306	0.000577107	0.000578229	0.00077123
1.080	0.0459504180	0.000375964	0.000377163	0.00050215
0.922	0.0964306261	0.000841848	0.000844498	0.00109934
0.757	0.0539821186	0.000361353	0.000362738	0.00047543
0.592	0.0485720478	0.000087705	0.000088360	0.00010153
0.430	0.0451860561	0.000062284	0.000062803	0.00007102
0.268	0.0524852095	0.000080898	0.000081587	0.00009477
0.095	0.0268969401	0.000008146	0.000008314	0.00003455
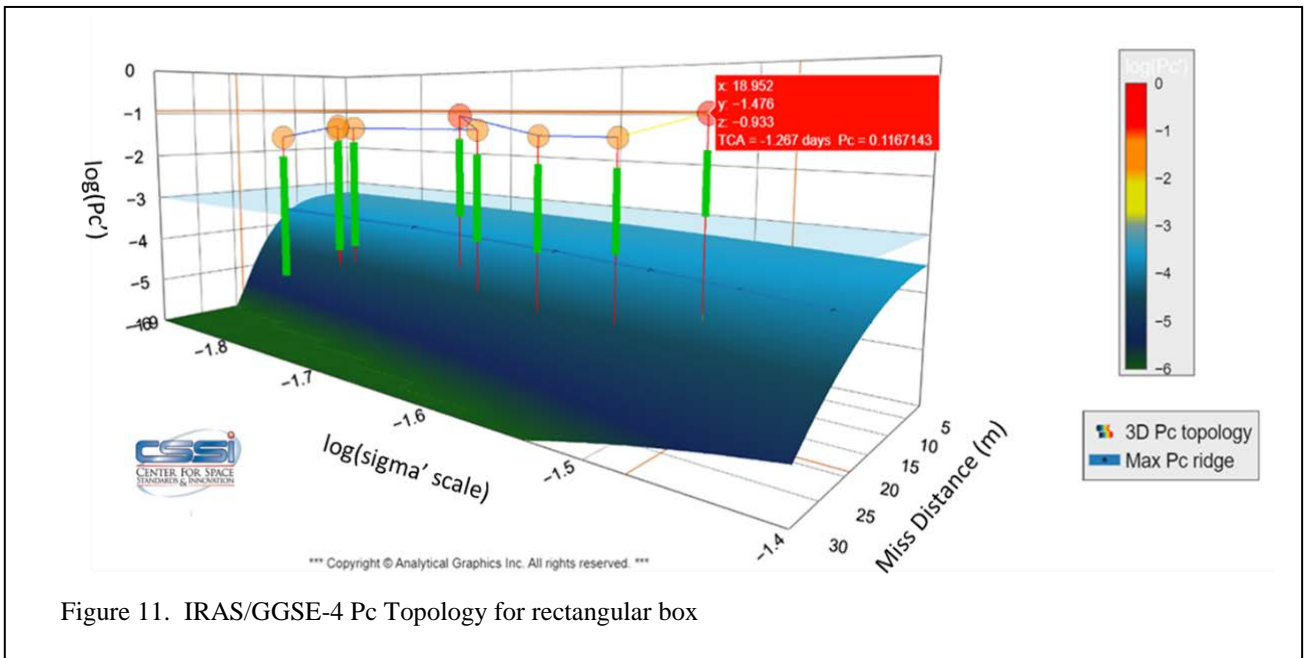
Figure 11. IRAS/GGSE-4 Pc Topology for rectangular box

Once again, the DEBBIE collision and explosion fragmentation tool was used to model the ensemble of debris fragments that could have been generated had this collision between two dead space objects occurred. For this simulation, we adopted a 30% involvement and a mass of 1063.43 kg by IRAS, and a 20% involvement and a mass of 85 kg by GGSE-4. From this DEBBIE simulation, it was estimated that 12,588 fragments larger than 1 cm in characteristic length could have generated from this collision. These individual fragments were each assigned notionally-representative post-fragmentation orbits.

Figure 12 portrays the resulting collision rate increase that could have been introduced by this potential collision. As before, the depiction shows the annual encounter rates solely from this collision-induced debris that augment Figure 9.

A key take-away from Figure 12 is that post-collision debris fragment collision rates at the collision's original altitude of 900 km above a spherical Earth are likely to increase fivefold. Note that these debris fragments will have orbital lifetimes of a hundred years or more, so this increased threat profile will be more or less a permanent degradation of our space operations threat profile.

Figure 12. Additional estimated annual collision rates resulting from IRAS/GGSE-4 simulated event.
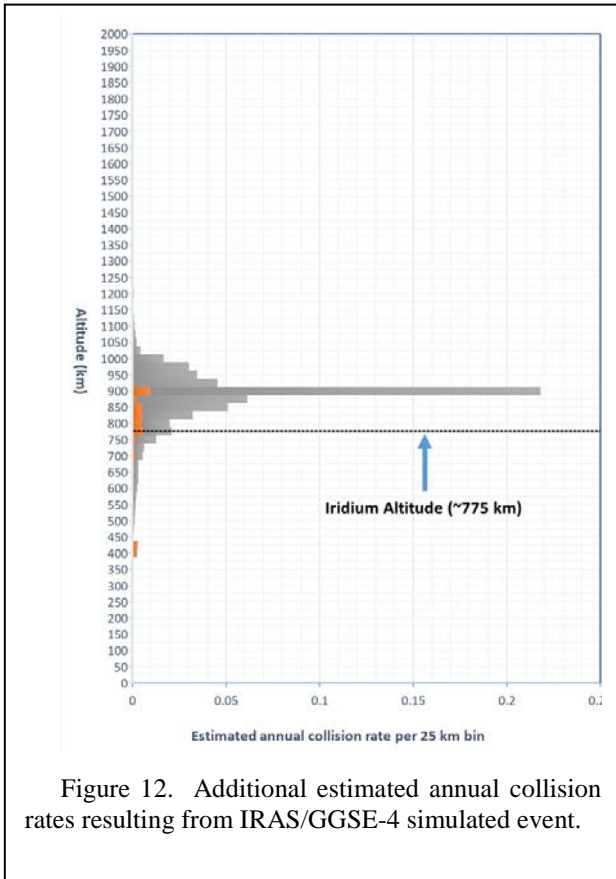
5. Conclusion

The New Space era is already here. As large constellation spacecraft quickly begin to dominate our active spacecraft population, the spacecraft operator community will increasingly need to rely upon an operationally-relevant, effective SSA and STCM enterprise that promotes our continued safe and effective use of outer space.

Results generated for the Aeolus/Starlink conjunction indicate that even as refined orbit estimates using advanced data analytics and orbit determination algorithms were employed, this conjunction remained at a high estimated threat level, warranting that a mitigation action (collision avoidance maneuver) be taken.

This example shows that in the absence of traffic rules and communication protocols, collision avoidance depends entirely on the pragmatism and close collaboration and cooperation of the operators involved. Yet today, this negotiation is done through exchanging emails - an archaic process that is no longer viable as increasing numbers of satellites in space mean more space traffic.

The assessment of collision risk and trending for the much publicized IRAS/GGSE-4 conjunction shows that while refined analyses show that this collision risk was decreasing, the long length of the GGSE-4 spacecraft yielded much variability in the collision probability metric as the GGSE-4 orientation varied across the encounter plane. Note that we did not adopt a traditional gravity-gradient-stabilized orientation in the above assessment.

6. Acknowledgment

We are grateful to the 18SPCS for authorizing the ComSpOC to incorporate raw Space Surveillance Network observations into the independently-generated, high-accuracy ComSpOC orbit solutions and derived conjunction assessments.

References:

[1] Stijn Lemmens and Francesca Letizia, "Environment Capacity as Driver for Space Traffic Management," IAA-UT-STM-02-05, 6th annual Space Traffic Management Conference, University of Texas at Austin, USA.

[2] Salvatore Alfano, Daniel L. Oltrogge, and Ryan Shepperd, "Leo Constellation Encounter and Collision Rate Estimation: An Update," IAA-ICSSA-20-0021, 2nd IAA Conference on Space Situational Awareness (ICSSA) Washington D.C., USA

[3] Salvatore Alfano and Daniel Oltrogge, "Probability of Collision: Valuation, Variability, Visualization, and Validity," Acta Astronautica, Volume 148, July 2018, pp. 301-316, DOI: 10.1016/j.actaastro.2018.04.023

[4] Yuchen Xie and Ken Chan, "Collision Probability for Rectangular Cross Sections," Paper No. AIAA 2018-2231, 2018 Space Flight Mechanics Meeting, Jan 9-12, 2018, Kissimmee, Florida.

[5] James L. Foster, J. and Herbert S. Estes, "A Parametric Analysis of Orbital Debris Collision Probability and Maneuver Rate for Space Vehicles," NASA/JSC-25898, August 1992.

[6] F. Kenneth Chan, "Collision Probability Analysis for Earth Orbiting Satellites," 7th International Space Conference of Pacific Basin Societies, Nagasaki, Japan, 1997.

[7] Salvatore Alfano, "A Numerical Implementation of Spherical Object Collision Probability," The Journal of the Astronautical Sciences, Vol. 53, No. 1, 2005, pp. 103–109.

[8] Russell P. Patera, "General Method for Calculating Satellite Collision Probability," Journal of Guidance, Control, and Dynamics, Vol. 24, No. 4, 2001, pp. 716–722. doi:10.2514/2.4771.

[9] Romain Serra, Denis Arzelier, Mioara Joldes, Jean-Bernard Lasserre, Aude Rondepierre and Bruno Salvy, "Fast and Accurate Computation of Orbital Collision Probability for Short-term Encounters," Journal of Guidance, Control, and Dynamics, Vol. 39, No. 5, 2016, pp. 1009–1021. doi:10.2514/1.G001353.

[10] Ricardo García-Pelayo and Javier Hernando-Ayuso, "Series for Collision Probability in Short-encounter Model," Journal of Guidance, Control, and Dynamics, Vol. 39, No. 8, 2016, pp. 1908–1916. doi:10.2514/1.G001754.

[11] Vincent T. Coppola, "Including Velocity Uncertainty in the Probability of Collision Between Space Objects," 22nd AAS/AIAA Space 341 Flight Mechanics Meeting, Charleston, SC, 2012.

[12] I. Carlvik, "Collision Probabilities for Finite Cylinders and Cuboids," Nuclear Science and Engineering, 30:1, 150-151, DOI: 10.13182/NSE30-01-150TN, 1967

[13] Ricardo Garcıa-Pelayo and Juan Luis Gonzalo, "Probability of collision between a rectangular cuboid and small debris," 5th CEAS Conference on Guidance, Navigation and Control, April 3-5, 2019, Milano, Italy.

[14] Georges Krier, "Satellite Collision Probability For Long-Term Encounters And Arbitrary Primary Satellite Shape," Proc. 7th European Conference on Space Debris, Darmstadt, Germany, 18–21 April 2017.

[15] Salvatore Alfano, "Accommodating Rectangular Objects in Probability Calculations," Paper No. AIAA 2004-5217, AAS/AIAA Astrodynamics Specialist Conference, Aug 16-19, 2004.

[16] Shuo Zhang, Tuo Fu, Defeng Chen and Huawei Cao, "Satellite Instantaneous Collision Probability Computation Using Equivalent Volume Cuboids," Journal of Guidance, Control, and Dynamics, June 2020, DOI: 10.2514/1.G004711.

[17] F Kenneth Chan, Spacecraft Collision Probability, El Segundo, CA, Aerospace Press, ©2008.

[18] Russell P. Patera, "Calculating Collision Probability for Arbitrary Space-Vehicle Shapes via Numerical Quadrature," Journal of Guidance, Control, and Dynamics, Vol. 28, No. 6, November-December 2005, pp. 1326-1328.

[19] Salvatore Alfano, "Eliminating Assumptions Regarding Satellite Conjunction Analysis," AAS Journal of the Astronautical Sciences, Vol. 59, Issue 4, December 2012, pp. 676–705. DOI: 10.1007/s40295-014-0002-4.

[20] Oltrogge, D.L., "Breakup Modeling With 1Earth's DEBBIE Module and STK," AGI User's Conference, Chicago IL, 7-10 October 2008.

[21] Finkleman, D., Oltrogge, D.L. Faulds, A. and Gerber, J.., "Analysis of The Response Of A Space Surveillance Network To Orbital Debris Events," Paper AAS 08-127, 2008 AAS/AIAA Astrodynamics Specialist Conference, Galveston, TX 27-31 January 2008.

[22] Salvatore Alfano and Daniel L. Oltrogge "Volumetric Assessment of Satellite Encounter Rates," Acta Astronautica, Volume 152, 2018, pp. 891-907, DOI: 10.1016/j.actaastro.2018.09.030.